Fast design of broadband terahertz diffusion metasurfaces

JIE ZHAO,[1,2] QIANG CHENG,[1,3,*] TIAN QI WANG,[1,2] WEI YUAN,[1,2] AND TIE JUN CUI[1,3,4]

[1]*State Key Laboratory of Millimeter Waves, Southeast University, Nanjing 210096, China*
[2]*Synergetic Innovation Center of Wireless Communication Technology, Southeast University, Nanjing 210096, China*
[3]*Cooperative Innovation Center of Terahertz Science, No. 4, Section 2, North Jianshe Road, Chengdu 610054, China*
[4]*tjcui@seu.edu.cn*
[*]*qiangcheng@seu.edu.cn*

Abstract: A method for fast design of broadband terahertz diffusion metasurface is presented. The proposed metasurface is composed by three kinds of simply patterned elements with different resonant properties. To obtain the best broadband performance with the lowest backward reflections, a genetic algorithm is developed to manipulate the resonances for the fast determination of element geometries. An inverse discrete Fourier transform method is used to predict the scattering pattern of the metasurface with high accuracy and low time consumption, significantly enhancing the efficiency of the array-pattern design. The proposed fast design flow will benefit a broad range of terahertz applications, such as biological detection and imaging.

References and links

1. N. Yu, P. Genevet, M. A. Kats, F. Aieta, J. P. Tetienne, F. Capasso, and Z. Gaburro, "Light propagation with phase discontinuities: generalized laws of reflection and refraction," Science **334**(6054), 333–337 (2011).
2. C. L. Holloway, E. F. Kuester, J. A. Gordon, J. O'Hara, J. Booth, and D. R. Smith, "An overview of the theory and applications of metasurfaces: the two-dimensional equivalents of metamaterials," IEEE Antennas Propag. Mag. **54**(2), 10–35 (2012).
3. H. Chen, C. T. Chan, and P. Sheng, "Transformation optics and metamaterials," Nat. Mater. **9**(5), 387–396 (2010).
4. J. B. Pendry, D. Schurig, and D. R. Smith, "Controlling electromagnetic fields," Science **312**(5781), 1780–1782 (2006).
5. S. Sun, K. Y. Yang, C. M. Wang, T. K. Juan, W. T. Chen, C. Y. Liao, Q. He, S. Xiao, W. T. Kung, G. Y. Guo, L. Zhou, and D. P. Tsai, "High-efficiency broadband anomalous reflection by gradient meta-surfaces," Nano Lett. **12**(12), 6223–6229 (2012).
6. Y. Zhao, X. Cao, J. Gao, X. Liu, and S. Li, "Jigsaw puzzle metasurface for multiple functions: polarization conversion, anomalous reflection and diffusion," Opt. Express **24**(10), 11208–11217 (2016).
7. T. J. Cui, S. Shuo Liu, and L. L. Lian, "Information entropy of coding metasurface," Light Sci. Appl. (to be published).
8. S. Liu, T. J. Cui, L. Zhang, Q. Xu, Q. Wang, X. Wan, J. Q. Gu, W. X. Tang, M. Qing Qi, J. G. Han, W. L. Zhang, X. Y. Zhou, and Q. Cheng, "Convolution operations on coding metasurface to reach flexible and continuous controls of terahertz beams," Adv Sci (Weinh) **3**(10), 1600156 (2016).
9. A. Arbabi, Y. Horie, M. Bagheri, and A. Faraon, "Dielectric metasurfaces for complete control of phase and polarization with subwavelength spatial resolution and high transmission," Nat. Nanotechnol. **10**(11), 937–943 (2015).
10. C. Pfeiffer and A. Grbic, "Millimeter-wave transmitarrays for wavefront and polarization control," IEEE Trans. Microw. Theory Tech. **61**(12), 4407–4417 (2013).
11. F. Aieta, P. Genevet, M. A. Kats, N. Yu, R. Blanchard, Z. Gaburro, and F. Capasso, "Aberration-free ultrathin flat lenses and axicons at telecom wavelengths based on plasmonic metasurfaces," Nano Lett. **12**(9), 4932–4936 (2012).
12. J. Kim, Y. M. Li, M. N. Miskiewicz, C. Oh, M. W. Kudenov, and M. J. Escuti, "Fabrication of ideal geometric-phase holograms with arbitrary wavefronts," Optica **2**(11), 958–964 (2015).

13. M. Paquay, J. C. Iriarte, I. Ederra, R. Gonzalo, and P. de Maagt, "Thin AMC structure for radar cross-section reduction," IEEE Trans. Antenn. Propag. **55**(12), 3630–3638 (2007).
14. S. Simms and V. Fusco, "Chessboard reflector for RCS reduction," Electron. Lett. **44**(4), 316–318 (2008).
15. J. C. I. Galarregui, A. T. Pereda, J. L. M. de Falcon, I. Ederra, R. Gonzalo, and P. de Maagt, "Broadband radar cross-section reduction using AMC technology," IEEE Trans. Antenn. Propag. **61**(12), 6136–6143 (2013).
16. W. G. Chen, C. A. Balanis, and C. R. Birtcher, "Checkerboard EBG surfaces for wideband radar cross section reduction," IEEE Trans. Antenn. Propag. **63**(6), 2636–2645 (2015).
17. Y. Q. Fu, Y. Q. Li, and N. C. Yuan, "Wideband Composite AMC surfaces for RCS Reduction," Microw. Opt. Technol. Lett. **53**(4), 712–715 (2011).
18. A. Edalati and K. Sarabandi, "Wideband, wide angle, polarization independent RCS reduction using nonabsorptive miniaturized-element frequency selective surfaces," IEEE Trans. Antenn. Propag. **62**(2), 747–754 (2014).
19. Y. C. Song, J. Ding, C. J. Guo, Y. H. Ren, and J. K. Zhang, "Ultra-broadband backscatter radar cross section reduction based on polarization-insensitive metasurface," IEEE Antennas Wirel. Propag. Lett. **15**, 329–331 (2016).
20. T. J. Cui, M. Q. Qi, X. Wan, J. Zhao, and Q. Cheng, "Coding metamaterials, digital metamaterials and programmable metamaterials," Light Sci. Appl. **3**(10), e218 (2014).
21. L. H. Gao, Q. Cheng, J. Yang, S. J. Ma, J. Zhao, S. Liu, H. B. Chen, Q. He, W. X. Jiang, H. F. Ma, Q. Y. Wen, L. J. Liang, B. B. Jin, W. W. Liu, L. Zhou, J. Q. Yao, P. H. Wu, and T. J. Cui, "Broadband diffusion of terahertz waves by multi-bit coding metasurfaces," Light Sci. Appl. **4**(9), e324 (2015).
22. D. S. Dong, J. Yang, Q. Cheng, J. Zhao, L. H. Gao, S. J. Ma, S. Liu, H. B. Chen, Q. He, W. W. Liu, Z. Fang, L. Zhou, and T. J. Cui, "Terahertz broadband low-reflection metasurface by controlling phase distributions," Adv. Opt. Mater. **3**(10), 1405–1410 (2015).
23. X. Yan, L. Liang, J. Yang, W. Liu, X. Ding, D. Xu, Y. Zhang, T. Cui, and J. Yao, "Broadband, wide-angle, low-scattering terahertz wave by a flexible 2-bit coding metasurface," Opt. Express **23**(22), 29128–29137 (2015).
24. Y. F. Li, J. Q. Zhang, S. B. Qu, J. F. Wang, H. Y. Chen, Z. Xu, and A. X. Zhang, "Wideband radar cross section reduction using two-dimensional phase gradient metasurfaces," Appl. Phys. Lett. **104**(22), 221110 (2014).
25. F. Costa, A. Monorchio, and G. Manara, "Wideband scattering diffusion by using diffraction of periodic surfaces and optimized unit cell geometries," Sci. Rep. **6**, 25458 (2016).
26. K. Wang, J. Zhao, Q. Cheng, D. S. Dong, and T. J. Cui, "Broadband and broad-angle low-scattering metasurface based on hybrid optimization algorithm," Sci. Rep. **4**, 5935 (2014).
27. M. Ohira, H. Deguchi, M. Tsuji, and H. Shigesawa, "Multiband single-layer frequency selective surface designed by combination of genetic algorithm and geometry-refinement technique," IEEE Trans. Antenn. Propag. **52**(11), 2925–2931 (2004).
28. P. Y. Chen, C. H. Chen, H. Wang, J. H. Tsai, and W. X. Ni, "Synthesis design of artificial magnetic metamaterials using a genetic algorithm," Opt. Express **16**(17), 12806–12818 (2008).
29. J. Zhao, Q. Cheng, J. Chen, M. Q. Qi, W. X. Jiang, and T. J. Cui, "A tunable metamaterial absorber using varactor diodes," New J. Phys. **15**(4), 043049 (2013).
30. H. T. Chen, J. Zhou, J. F. O'Hara, F. Chen, A. K. Azad, and A. J. Taylor, "Antireflection coating using metamaterials and identification of its mechanism," Phys. Rev. Lett. **105**(7), 073901 (2010).
31. J. Zhao, Q. Cheng, X. K. Wang, M. J. Yuan, X. Zhou, X. J. Fu, M. Q. Qi, S. Liu, H. B. Chen, Y. Zhang, and T. J. Cui, "Controlling the bandwidth of terahertz low-scattering metasurfaces," Adv. Opt. Mater. **4**(11), 1773–1779 (2016).
32. K. K. Yan and Y. L. Lu, "Sidelobe reduction in array-pattern synthesis using genetic algorithm," IEEE Antennas Propag. Mag. **45**(7), 1117–1122 (1997).
33. R. L. Haupt, "An introduction to genetic algorithms for electromagnetics," IEEE Antennas Propag. Mag. **37**(2), 7–15 (1995).
34. W. P. M. N. Keizer, "Fast low-sidelobe synthesis for large planar array antennas utilizing successive fast Fourier transforms of the array factor," IEEE Trans. Antenn. Propag. **55**(3), 715–722 (2007).

1. Introduction

In the past few years, it has been demonstrated that artificial metasurfaces could provide an unprecedented way to control electromagnetic (EM) waves [1–4], enabling many applications in microwave/optical engineering, such as anomalous reflection, polarization splitting, ultrathin lenses, and optical holography [5–12]. Low-scattering or diffusion metasurfaces have received increasing attention because of their potential applications in imaging, biological detection and wireless communication. A simple route to achieve backward-scattering suppression was implemented using a chessboard-like surface composed of combinations of perfect electric-conductor (PEC) elements and artificial magnetic-conductor (AMC) elements with opposite reflected phases [13,14]. Due to the strong destructive interference from the elements along the surface, the incident beam can be efficiently split

into four reflection beams away from the incoming direction, leading to significant decrease of backward energy within a narrow bandwidth.

By replacing the PEC element with another AMC element [15–17], the condition for destructive interference can also be satisfied at the different resonance frequencies of the two AMC structures, thus expanding the working bandwidth or obtaining a dual-band property. However, the large side lobes in these designs would result in high detection possibilities for bistatic systems due to the regular arrangement of elements. To further suppress the undesired side lobes, the metasurfaces are constructed using elements with random reflected phases that mimic rough surfaces, where the incident wave is diffusely reflected without any specific direction [18].

Up to now, more and more research efforts have been devoted to the design of broadband diffusion metasurface in the microwave and terahertz spectrum [19–23], where many complicated geometries and optimization methods have been introduced regarding the designs of broadband metasurfaces [24–26]. However, in all the published works, the design procedures are still time-consuming to get the low scattering performance, which calls for faster algorithms in the element selection and array pattern determination.

To speed up the design flow, two measures have been taken in this paper: One is to choose element with simple geometries, where the combination of multi-resonances are utilized to broaden the bandwidth with the help of the genetic algorithm (GA), leading to the rapid determination of the element dimensions. The other is the fast optimization of array pattern based on two-dimensional inverse discrete Fourier transform (2D IDFT), which can greatly reduce the burden of the computation time and memory sources. To validate the design criterions, a terahertz diffusion metasurface is fabricated and experimentally characterized. Good agreements have been achieved between the simulated and measured results, showing the applicability and effectiveness of the proposed method.
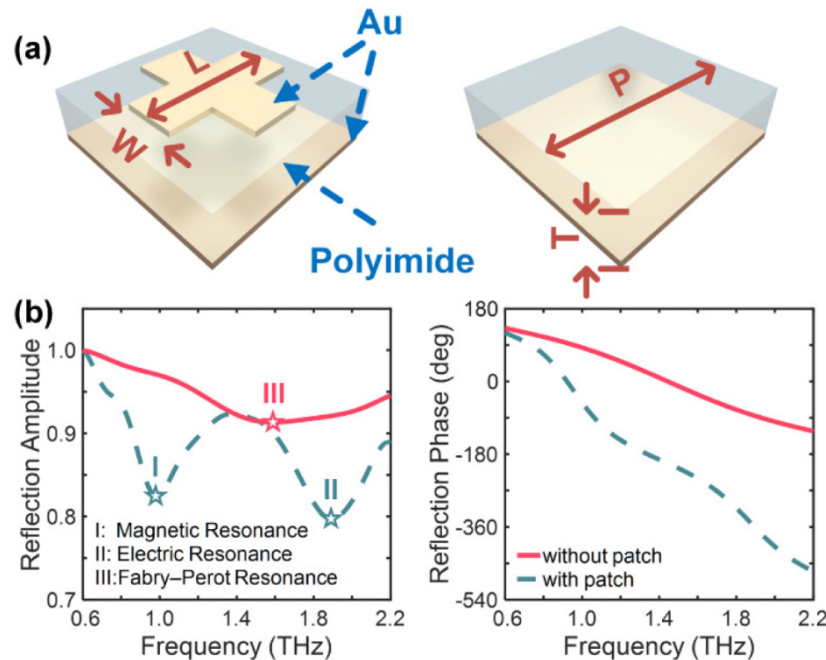

Fig. 1. (a) Schematic of the cross patch element and the bare element. (b) The corresponding reflection amplitude (left) and phase (right) for the cross patch element (dashed line) and the bare element (solid line). I, II, and III represent the magnetic resonance, the electric resonance, and the Fabry-Perot resonance respectively.

2. Element design and optimization

In previous papers, a number of structures with broadband features have been proposed and discussed in detail. However, due to the complexity of the geometries [24], it is prohibitively time consuming to determine the element dimensions. In some cases, the optimization method is used to find the element with ideal performance [25,27,28], where the element is divided into $M \times N$ regular array pixels, and each pixel is either filled with a PEC patch or left bare. This method is computationally intensive, as there are approximately $2^{N \times M}$ possibilities for the pixel pattern. Also the complicated element geometry can lead to fabrication challenges especially in the terahertz, infrared, or higher frequency region.

In fact, it is possible to obtain broadband meta-atoms with simple element geometries, in which the electric resonance (ER) and magnetic resonance (MR) of the elements should be adjusted carefully to get the desired bandwidth. Here considering a bare element with only dielectric layer and metallic background (right in Fig. 1(a)), the simulated reflection based on CST Microwave Studio at normal incidence is plotted with red solid lines in Fig. 1(b), where a Fabry-Perot (F-P) resonance is generated. In the simulation, the metal is Au with the thickness of 160 nm and the electric conductivity of $4.56 \times 10^7 \, \text{S/m}$; the dielectric is polyimide with the relative permittivity of $3 \cdot (1 - j0.03)$; the boundary conditions at the two orthogonal directions (X and Y direction; the wave is propagating along –Z direction) are set to be perfect electric conductor and perfect magnetic conductor respectively [22,26]; the mesh size is $1/20\lambda$ at the central frequency (1.4 THz). For comparison, the reflection curve for the element with a cross patch pattern (left in Fig. 1(a)) is also plotted in Fig. 1(b), with green dashed lines. Two resonances could be observed in this case, where the ER emerges at the higher frequency, and the MR appears at the lower frequency, originating from the loop currents flowing between the upper patch and the background metal [29]. Actually, the bandwidth of the diffusion metasurface can be expanded if the electric-resonance frequency (ERF) and the magnetic-resonance frequency (MRF) are located within the proper spectral interval. Although only one type of resonance is shown for the bare element, it has the advantages of lower loss and flatter phase slope than element with cross patch. Additionally, the F-P resonance frequency (FPRF) of the bare element lies between the MRF and ERF of the cross patch element, making it possible to compensate the deteriorated performance between the two frequencies for final designed metasurface.

To maintain the broadband property for bare element, a suitable thickness of the substrate (polyimide) layer is necessary to ensure that the resonance frequency lies in the working spectrum of interest. From the electromagnetic theory, the reflection for bare element can be expressed as [30]

$$
\begin{aligned}
r_{bare\ element} &= r_{12} - \frac{t_{12}t_{21}\exp(-2jkd)}{1+r_{21}\exp(-2jkd)} \\
&= \frac{\left(1-\sqrt{\varepsilon_{poly}}\right)-\left(1+\sqrt{\varepsilon_{poly}}\right)\exp(-2jkd)}{\left(1+\sqrt{\varepsilon_{poly}}\right)-\left(1-\sqrt{\varepsilon_{poly}}\right)\exp(-2jkd)}.
\end{aligned}
\tag{1}
$$

where r_{12} and t_{12} are the reflection and transmission coefficients between air and the polyimide layer, and r_{21} and t_{21} are just the opposite; k is the wavenumber in the polyimide; d denotes the substrate thickness, and $\varepsilon_{poly} = 3 \cdot (1 - j0.03)$ is the relative permittivity of the polyimide. From Eq. (1), different resonant frequency usually requires different substrate thickness for minimum reflection, e.g., for 1 THz, the thickness is 43.3 μm; while for 2 THz, it changes to 21.6 μm. In our design, we wish to cover the spectral range from 1 THz to 2

THz, which means that the thickness should lies between 21.6 μm and 43.3 μm. As a trade-off, the thickness of 30 μm ($\approx \sqrt{21.6 \times 43.3}um$) is an appropriate choice.
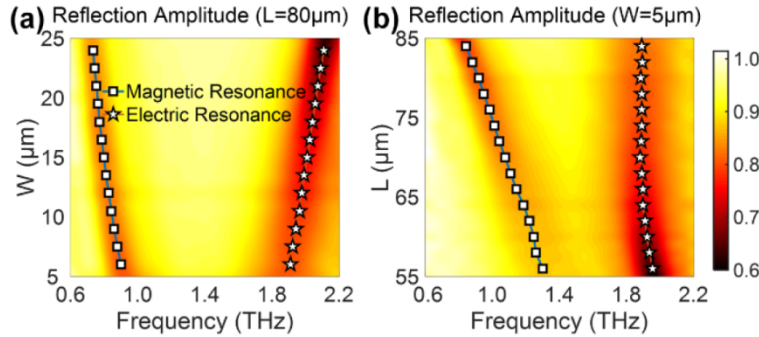

Fig. 2. The relationship between the reflection amplitude and the geometric parameter (a) *W* and (b) *L* for the cross patch element. The squares and stars represent the magnetic resonance and the electric resonance respectively.

To characterize the MRF and ERF of an element with a cross patch, numerical simulations are performed first to find the relationship between the reflectivity and the geometric dimensions (the width (*W*) and the length (*L*) in Fig. 1(a)). Here the period of the element is 88 μm. The simulated reflection amplitude is shown in Figs. 2(a) and 2(b), in which the square and star markers represent the MR and ER, respectively. It is obvious that the ERF changes with the increase of *W* but nearly remain unchanged when *L* is varied, while the MRF mainly depends on *L*. Thus, the cross resonator permits the control of MRF and ERF conveniently.

In our design, the whole metasurface is composed by three kinds of elements, where two of them are cross patch elements and the remaining is the bare element, as denoted by E1, E2 and E3. As mentioned above, there are altogether five resonance frequencies for these three elements, namely, *MRF1*, *ERF1*, *MRF2*, *ERF2* and *FPRF3*, which should be carefully arranged within the working spectrum to broaden the bandwidth and generate necessary phase differences for destructive interference along the metasurface. For simplicity, the inequality is supposed to be satisfied for the five resonance frequencies

$$MRF_1 < MRF_2 < FPRF_3 < ERF_1 < ERF_2. \tag{2}$$

The orders of the resonances for E1-E3 in Eq. (2) are our assumption based on the practical element design, which might help to reduce the computation time as well as acquire the broadest bandwidth. For example, if we assume $MRF_1 < MRF_2$, one possible set of geometric parameters can be chosen as $P = 88$ μm, $L_2 = 63$ μm $< L_1 = 83$ μm. It is easy to tell from numerical simulations (not shown here) that ERF_1 would change from 1.86 THz to 2.14 THz when W_1 varies from 5 μm to 25 μm, while ERF_2 would change from 1.90 THz to 2.16 THz when W_2 varies from 5 μm to 25 μm. By properly selecting W_1, W_2 in the design, it is possible to obtain a smaller ERF for E1, and a higher ERF for E2, that is, $ERF_1 < ERF_2$, to have the largest bandwidth up to 2.16 THz in this case.

According to the fabrication considerations, such inequality usually requires:

$$5\mu m \le W_1 \le W_2 \le L_2 - 5\mu m \le L_1 \le P - 5\mu m, \left(50\mu m \le P \le 100\mu m\right). \tag{3}$$

In addition, the electromagnetic responses from the three elements are also closely related to the backward reflectivity of the metasurface, as pointed out in [31]. For example, in the normal direction,

$$R_{backward} = \left|\sum_i a_i \cdot r_i\right|^2, \left(i = 1, 2, 3\right). \tag{4}$$

where $R_{backward}$ is the backward-reflected energy, a_i is the proportion of areas for element i, and r_i is the reflection of element i. To further simplify the model, it is assumed that the proportions of all elements are equal since we want to utilize the destructive interference among the elements with specific phase relations in such configuration to make the reflection coefficient of the metasurface approaching −10 dB [31]. To further simplify the model, it is assumed that the proportions of all elements are equal. It is clear that the geometric dimensions of the elements E1-E2 should be optimized to satisfy the inequality Eq. (3) to get the largest bandwidth and in the meantime obtain the lowest reflectivity from Eq. (4).

To fulfill this purpose, a GA method is adopted to implement the geometry optimization [32,33], which concerns five parameters: the period (P) of the elements, the length (L_1) and width (W_1) of E_1, and the length (L_2) and width (W_2) of E2. The design-flow for the optimization of the element dimensions is demonstrated in Fig. 3. First, the population is initialized based on Eq. (3). Second, the fitness of the initial population is evaluated with the help of the commercial full-wave simulation software CST Microwave Studio. Then, if the termination criterion is satisfied, the optimization procedure ends; otherwise, the individuals with good value of fitness are selected and are updated by the crossover & mutation procedure to generate the next population, which satisfies the requirement in Eq. (3). The same procedure is carried out until the desired result is obtained. The fitness function can be written as:

$$fitness = 100 \times \int_{0.8}^{2.1} (dBR - g_1) \cdot g_2 \, df \ (\text{dB} \cdot \text{THz}).$$ (5)

where

$$dBR = \text{dB}(R_{backward}).$$ (6)

$$g_1(f) = \begin{cases} -10\,\text{dB}, & 0.8\,\text{THz} \le f < 1.0\,\text{THz} \\ -12.5\,\text{dB}, & 1.0\,\text{THz} \le f < 1.4\,\text{THz} \\ -11\,\text{dB}, & 1.5\,\text{THz} \le f < 2.0\,\text{THz} \\ -10\,\text{dB}, & 2.0\,\text{THz} \le f \le 2.1\,\text{THz} \end{cases}.$$ (7)

$$g_2(f) = \begin{cases} 1, & dBR > g_1 \\ 0, & dBR \le g_1 \end{cases}.$$ (8)
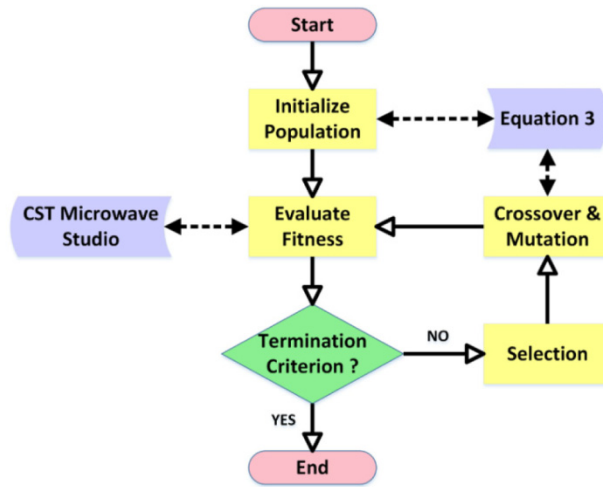

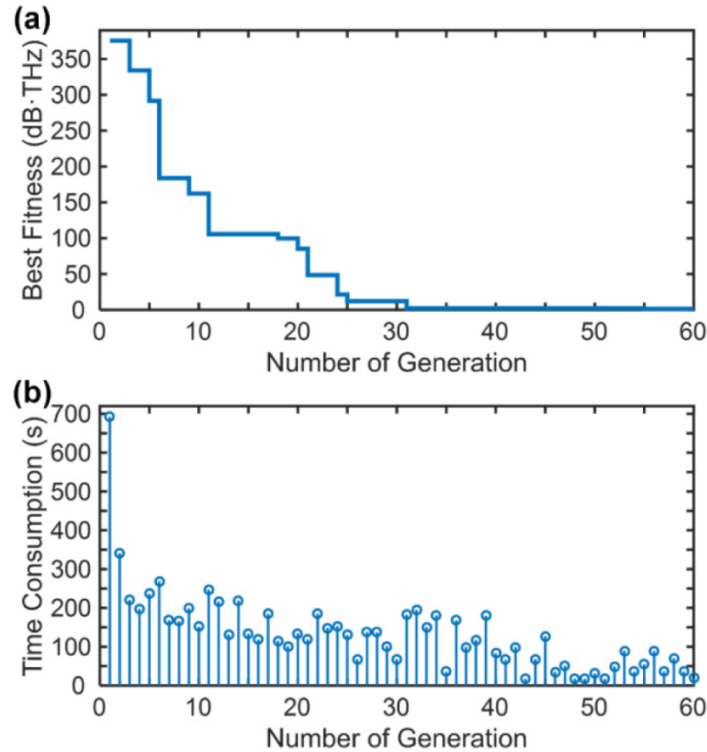Fig. 3. Design-flow for the element optimization based on GA.

Fig. 4. The progression of (a) the best fitness value and (b) the time consumption during the optimization procedure.

The optimization targets to ensure that the reflected energy is sufficiently small over a wide spectrum. The geometric parameters to be optimized can be divided into two subgroups: (P, L_1, and W_1) for E1; and (P, L_2, and W_2) for E2. For each individual, the numerical simulation (based on CST Microwave Studio) should be carried out twice to determine the reflections for E1 and E2. As the reflection for E3 does not change in the optimization process, the time consumption for E3 needs not to be taken into account. It takes approximately 18 s to perform the simulation for one element based on a desktop with the i7-4790 Intel Core and the 8 GB memory. When the size of the population is selected to be 20, the time for one iteration is approximately 720 s. If the maximum number of iterations is 60, the total time consumption is approximately 43200 s (12 h).

However, since the same subgroup might exist in different individuals or different iterations, the total simulation time can be reduced significantly. For every simulation, the data for reflection can be stored in the hard disk. In the simulation of a new individual, if an element with the same subgroup parameters has already been simulated, the results can be read from the hard disk directly to save approximately 18 s of computation time.
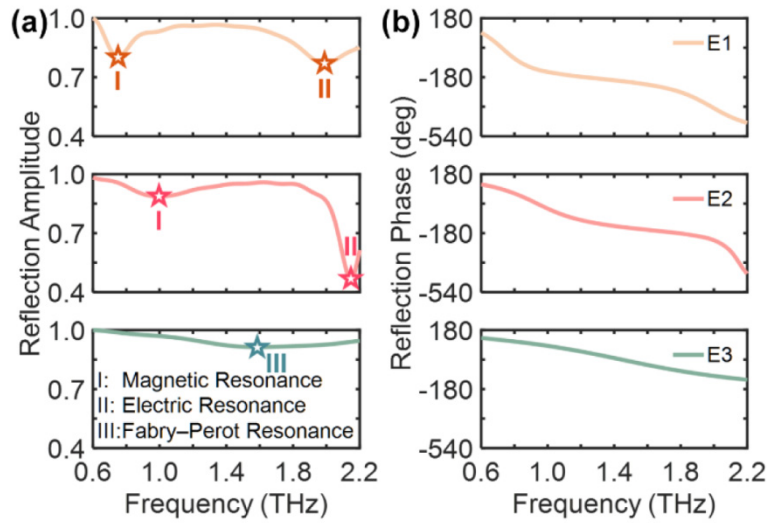
Fig. 5. (a) Reflection amplitude and (b) phase spectra for elements E1-E3.

Table 1. Structural parameters of the basic elements E1-E3.

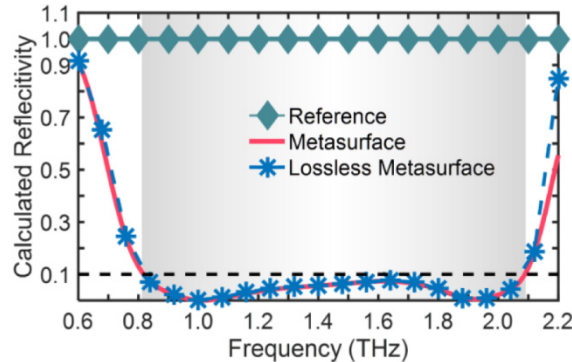| Element No.	P (um)	L (um)	W (um)	T (um)
E1	88	83	14	30
E2	88	63	23	30
E3	88	0	0	30

Fig. 6. Calculated normalized reflectivity for the metasurface and the lossless metasurface in the spectrum range from 0.6 THz to 2.2 THz under normal incidence.

Figure 4(a) shows the best value of the fitness function over different iterations (generations), which decreases from more than 350 to approximately 2 after 32 iterations. The time consumption for the first generation is approximately 700 s, and the simulation data are saved, which helps to reduce the time consumption in the next generation significantly. The total time consumption for all 60 iterations is 12188 s (3.39 h), far shorter than the original simulation time (12 h).

The optimized geometric dimensions of the elements E1-E3 are listed in Table 1, with the corresponding reflection coefficients shown in Fig. 5. All elements exhibit high reflectivity from 0.6 THz to 2.2 THz, except E2 at 2.15 THz, which is outside the bandwidth of interest. The MRFs of E1 and E2 are lower than the FPRF of E3, while the ERFs are higher as expected. The phase range of E1 and E2 approaches 720° over the whole spectrum from the confluence of both ER and MR, while the phase range of E3 is only 360° based on the F-P resonance. The phase curves show good linearity for all the elements after optimization. The

calculated reflectivity based on Eq. (4) is illustrated by a red solid line in Fig. 6, where broadband property is exhibited from 0.81 THz to 2.09 THz, with the normalized calculated reflectivity less than 0.1 (or −10 dB) with respect to a reference (PEC) plate of the same size. To consider the influence of material loss (mainly caused by the polyimide layer) for all the elements, the calculated reflectivity for lossless case (the reflection amplitudes for E1-E3 are set as 1) are also shown by a blue dashed line in Fig. 6 for comparison, which is consistent with the red solid lines, indicating that the current material loss does not affect the overall performance of metasurface greatly.

3. Optimization of array pattern

Although the backward reflectivity of the metasurface is reduced to be ultra-low in a broad spectral range as stated in previous section by choosing proper elements, it is still necessary to avoid significant enhancement of the side lobes of the scattering pattern that is important for stealth applications. Therefore, two methods have been put forward to synthesize the array pattern for side-lobe suppression [26]. One is based on full-wave simulation, with extremely high cost of computation time and computer memory. The other starts from the theory of antenna array, with the scattering pattern expressed by superposition from the contributions of all the elements:

$$\vec{E}_{total} = \sum_m \sum_n \vec{E}_{m,n} \cdot \exp\left[jk_0 \left(m \cdot d_x \cdot \sin\theta \cdot \cos\varphi + n \cdot d_y \cdot \sin\theta \cdot \sin\varphi \right) \right]. \quad (9)$$

where $\vec{E}_{total}$ is the electric far-field pattern of the whole metasurface; $\vec{E}_{m,n}$ is the electric far-field pattern of element (m, n); θ and φ are the elevation and azimuth angles, respectively; d_x and d_y are the periods of the elements along the x and y directions, respectively; k_0 is the wave number in free space. However, when the number of the elements within the metasurface increase dramatically, the time consumption from Eq. (9) becomes prohibitive and unacceptable. To overcome the deficiency, a 2D IDFT method is introduced to accelerate the calculation [34]. As the dimensions of the basic elements are much smaller than the wavelength, we can assume that all the elements have the same scattering pattern with various amplitude and phase, which are weighted as follows:

$$\vec{E}_2 = a_2 \exp\left(j\varphi_2\right) \cdot \vec{E}_1, \quad \vec{E}_3 = a_3 \exp\left(j\varphi_3\right) \cdot \vec{E}_1. \quad (10)$$

Substituting Eq. (10) into Eq. (9), we have

$$\vec{E}_{total} = \vec{E}_1 \cdot \sum_m \sum_n I_{m,n} \cdot \exp\left[jk_0 \left(m \cdot d_x \cdot \sin\theta \cdot \cos\varphi + n \cdot d_y \cdot \sin\theta \cdot \sin\varphi \right) \right]$$
$$= \vec{E}_1 \cdot AF. \quad (11)$$

where $\vec{E}_1$ is the element factor, $I_{m,n} = a_{m,n} \exp\left(j\varphi_{m,n}\right)$, and AF is the array factor. Suppose that

$$u = \sin\theta \cdot \cos\varphi, \quad v = \sin\theta \cdot \sin\varphi. \quad (12)$$

$$p = \frac{M \cdot d_x \cdot k_0 \cdot u}{2\pi}, \quad q = \frac{N \cdot d_y \cdot k_0 \cdot v}{2\pi}. \quad (13)$$

the array factor can then be expressed as

$$AF = \sum_m \sum_n I_{m,n} \cdot \exp\left(j\frac{2mp\pi}{M} \right) \cdot \exp\left(j\frac{2nq\pi}{N} \right)$$
$$= M \cdot N \cdot \text{IDFT2}\left(I_{m,n}\right). \quad (14)$$
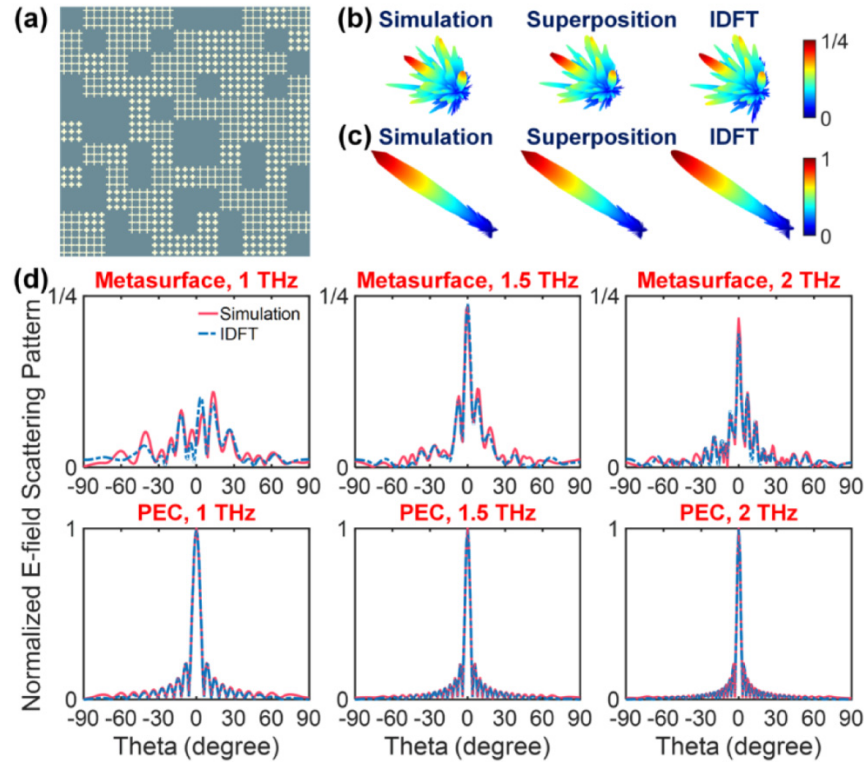
where IDFT2 is the 2D IDFT.

Fig. 7. (a) Schematic of the optimized array pattern. Scattering patterns of (b) the metasurface and (c) the PEC plate of the same dimension, based on full-wave simulation, superposition, and IDFT method. (d) Full-wave simulated results (red solid lines) and IDFT results (blue dashed lines) of the electric-field scattering patterns in the E-plane for the designed metasurface and PEC plate.

To eliminate the large side lobes, a particle swarm optimization (PSO) method is utilized together with the IDFT method to achieve the optimal arrangement of meta-atoms. As shown in Fig. 7(a), the total metasurface is composed by three kinds of super-lattices, which are constituted by 3×3 arrays of E1, E2 and E3 respectively. Such configuration can help to comply with the hypothesis of the periodic boundary condition. There are altogether 121 super-lattices in the finally optimized metasurface, covering the area of 2904 μm^2. The three dimensional scattering pattern simulated by the full-wave electromagnetic solver (CST Microwave Studio), and that calculated using the superposition method and IDFT method are presented in Fig. 7(b) for comparison, showing excellent agreement which demonstrates the validity of the fast prediction method described above. Figure 7(c) is the normalized scattering pattern of a PEC plate with the same dimension. The time consumption for all the three methods varies greatly: the full wave simulation, superposition method and IDFT method cost 3 h, 150 s, and 0.1 s, respectively.

To further investigate the difference of the results from the three methods, the scattering patterns in the E-plane are plotted in Fig. 7(d) at 1 THz, 1.5 THz and 2 THz respectively. The discrepancy is concentrated at low frequencies, since the influence from the aperiodic boundary can no longer be neglected with the increase of the wavelength, incompatible to the periodic boundary hypothesis in the element simulation.
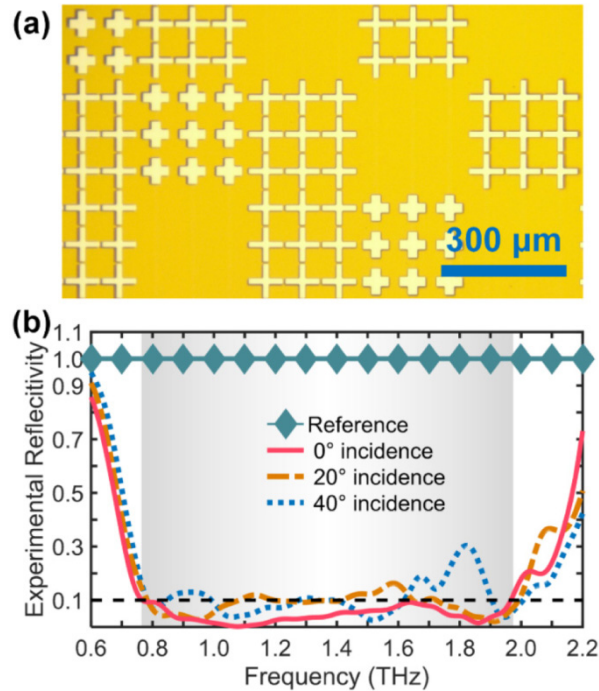
Fig. 8. (a) Photograph of the fabricated metasurface sample. (b) The measured specular reflection spectra of the metasurface from 0.6 to 2.2 THz at incident angles of 0°, 20°, and 40°.

Table 2. Experimental results of this paper and previous works.

Ref.	Spectrum Start	Spectrum Stop	Relative Bandwidth	Suppression	Thickness
This work	0.77 THz	1.97 THz	**87.6%**	≥90%	30 um
Ref [21].	0.8 THz	1.8 THz	76.9%	≥90%	30 um
Ref [22].	1.1 THz	1.8 THz	48.3%	≥90%	30 um
Ref [23].	0.8 THz	1.5 THz	60.9%	≥90%	40 um
Ref [31].	0.59 THz	1.29 THz	74.5%	≥88.9%	30 um

4. Experiment and discussion

To validate the design procedures mentioned above, a terahertz metasurface is fabricated through photolithography, whose magnified shot are illustrated in Fig. 8(a). A commercial terahertz time-domain spectroscopic system (TDS, Zomega-Z3, USA) is employed to measure the reflectivity of the metasurface for normal and oblique incidence. The experimental results (Fig. 8(b)) show that the reflectivity is below 0.1 from 0.77 THz to 1.97 THz, slightly deviated from the calculated results (0.81 THz to 2.09 THz), which might originate from the drawback of material characterization and experimental environment. The permittivity of the fabricated polyimide layer might have little deviation from that used in simulation. The signal-to-noise ratio (SNR) of the TDS we used is poor above 2 THz, which may impact the measured results at high frequencies negatively in Fig. 8(b). The specular reflectivity under oblique incidence are also presented in Fig. 8(b) with the incident angle varying from 20° to 40°, showing slightly narrowing of the bandwidth and tiny increase of the total reflectivity, which is consistent with other published works [21–23].

Compared with previous research with the same substrate parameters, our design achieves the best experimental results, with the relative bandwidth reaching 87.6%, as shown in Table 2 [21–23,31]. This improved performance can be attributed to the following factors: 1. The

structures of the multi-resonances in the previous work are too complex to achieve ideal performance. In our design, the MR and ER of an element with a simple structure can be tuned conveniently. Additionally, we use the GA method to obtain the best bandwidth. 2. The cross patch is easier to fabricate than the complicated structure elements used in the other works in the terahertz region with less manufacturing errors. In general, a number of benefits are offered by our design, including large bandwidth, high design efficiency and low fabrication difficulty, showing great potential for biological detection and imaging applications in the future.

5. Summary

We have proposed a method for fast design of the diffusion metasurfaces, where the time consumption is significantly reduced compared to previous research based on two aspects: one is the adoption of elements with simple geometry, taking advantage of different resonance properties together with GA optimization method to achieve the best broadband performance. The other is the fast prediction of the scattering pattern of the whole metasurface based on IDFT that greatly facilitates the rapid determination of array pattern. This method is validated experimentally, showing excellent backward scattering from 0.77 THz to 1.97 THz, which is better than the bandwidth reported in previously published works with the same substrate parameters.

Funding